Effect of Processing Parameters on Microstructure and Mechanical Properties of an Al-$Al_{11}Ce_3$-Al_2O_3 *In-Situ* Composite Produced by Friction Stir Processing

C.F. CHEN, P.W. KAO, L.W. CHANG, and N.J. HO

Friction stir processing (FSP) was applied to produce aluminum-based *in-situ* composites from powder mixtures of Al-5 mol pct CeO_2. A billet of powder mixtures was prepared using the conventional pressing and sintering route. The sintered billet was then subjected to multiple passages of FSP. This technique has combined the hot-working nature of FSP and the exothermic reaction between Al and CeO_2. The reinforcing phases were identified as $Al_{11}Ce_3$ and δ^*-Al_2O_3. The Al_2O_3 particles with an average size of ~10 nm are uniformly distributed in the aluminum matrix, which has an average grain size of approximately 390 to 500 nm. Both the sintering temperature and the tool traversing speed used in FSP have significant influence on the microstructure and mechanical properties of the composite. The composite produced by sintering at 833 K followed by FSP with a tool traversing speed of 30 mm/min possesses an enhanced modulus ($E = 109$ GPa) and strength (ultimate tensile strength (UTS) = 488 MPa) as well as a tensile ductility of ~3 pct.

DOI: 10.1007/s11661-009-0115-8

I. INTRODUCTION

FRICTION stir processing (FSP) for the microstructural modification of materials was developed based on the principle of friction stir welding (FSW).[1] Mishra and Ma have completed a comprehensive literature review on FSW and FSP.[2] In a recent review article,[3] Ma addressed the current state of the understanding and development of FSP. A variety of effective FSP applications have been shown, as follows: (1) homogenizing the microstructure of Al-based nanocomposites,[4,5] (2) producing Al alloys with an ultrafine-grained structure[6–8] and Mg alloys,[9] (3) fabricating a fine-grained superplastic microstructure,[10,11] (4) refining the microstructure of cast-aluminum alloys,[12–15] (5) forming a surface composite on an aluminum substrate,[16] (6) forming an *in-situ* metal matrix composite,[17–20] *etc.*

It is widely recognized that the mechanical properties of metal matrix composites (MMCs) are controlled by the size and volume fraction of the reinforcements as well as the nature of the matrix-reinforcement interface.[21] Superior mechanical properties can be achieved when fine and stable reinforcements with good interfacial bonding are dispersed uniformly in the matrix. In conventionally produced particulate-reinforced MMCs, the size of reinforcement particles is normally much larger than 1 μm and the particles are located intergranularly in the metal matrix. Therefore, they cannot contribute to the strength by the Orowan mechanism. However, for composites with a large amount of nanometer-sized particles, which are distributed both intragranularly and intergranularly, the interparticle spacing may be reduced to the order of 100 nm or less, and the matrix grain size may be limited to the submicrometer range due to the Zener pinning effect.[22] The contributions due to the Orowan strengthening and the grain-size strengthening can then be very significant.

In general, the reinforcing particles used in MMCs are formed prior to their addition to the matrix metal. In this case, the scale of the reinforcing phase is limited by the starting particle size, which is typically of the order of microns to tens of microns and is rarely below 1 μm. Other drawbacks for the conventionally processed MMCs that have to be overcome are poor interfacial bonding and poor wettability between the reinforcement and the matrix due to surface contamination of the reinforcements. A possible alternative is to synthesize the reinforcement *in situ* in the metal matrix.[23]

Recent research work[17–19] has shown that *in-situ* aluminum matrix composites can be fabricated by FSP without a further consolidation process. The basic idea for fabricating the *in-situ* composites is to combine the hot-working nature of FSP and the exothermic reaction between aluminum and transition metals. The FSP provides the following functions:[17] (1) severe plastic deformation, to promote mixing and refining of constituent phases in the material; (2) elevated temperature, to facilitate the *in-situ* reaction; and (3) hot consolidation, to form a fully dense solid. The FSP has been successfully applied to produce intermetallic-reinforced aluminum matrix composites from elemental powder mixtures of Al-Cu, Al-Ti, and Al-Fe.[17–19]

C.F. CHEN, Graduate Student, P.W. KAO, Professor, L.W. CHANG, Associate Professor, and N.J. HO, Professor, are with the Department of Materials and Optoelectronics Science, Center for Nanoscience and Nanotechnology, National Sun Yat-Sen University, Kaoshiung 804, Taiwan R.O.C. Contact e-mail: pwkao@mail.nsysu.edu.tw

Manuscript submitted February 17, 2009.
Article published online December 2, 2009

Thermite reactions can occur between aluminum and an oxide of a less reactive metal, and stable Al_2O_3 will be formed. Consequently, aluminum matrix composites reinforced by Al_2O_3 particles can be produced by oxide-aluminum displacement reaction. The Al-Al_2O_3 *in-situ* composites have been produced in many Al-oxide systems, such as Al-Fe_2O_3,[24] Al-CuO,[25] and Al-SiO_2.[26] In the present work, the idea of forming an *in-situ* composite *via* FSP was applied to the Al-metal oxide (MO) system. Because the heat release of the Al-MO reaction is much higher than that of the Al-transition metal (Al-TM), a higher temperature and an enhanced reaction rate are expected from the Al-MO reaction. Because of the stability of Al_2O_3 in aluminum, fine Al_2O_3 particles are expected from this process. In this work, CeO_2 was selected to react with Al to form the *in-situ* composite. In addition to Al_2O_3, the Ce reduced from CeO_2 will also react with Al to form an intermetallic compound, $Al_{11}Ce_3$. Because Ce has low diffusivity and solubility in aluminum,[27] the $Al_{11}Ce_3$ compound is also expected to have a low coarsening rate at an elevated temperature.

The conventional pressing and sintering route was used to form a precursor from a powder mixture of constituents. The main purpose of sintering is to provide enough strength to prevent fracture as the rotating tool plunges into it during FSP. However, depending upon the temperature, different degrees of reaction may occur during sintering.

In FSP, the major processing parameters are the tool rotating rate and the tool traversing speed. The intense plastic deformation around the tool and the friction between the tool and the workpiece both contribute to the temperature increase in the stirred zone (SZ). The maximum temperature in the SZ during FSW of various aluminum alloys was reported to be between 0.6 and 0.9 T_m.[2] Generally, an increase in the ratio of the rotation rate to the traversing speed will increase the peak temperature in FSP. In the present case, the heat release due to the *in-situ* chemical reaction in FSP can also contribute to the temperature rise. In the present study, the effect of the sintering temperature and the tool traversing speed on the microstructure and mechanical properties of the composites was investigated.

II. EXPERIMENTAL

The starting materials used are pure aluminum powder (99.7 pct purity, average size 40 μm) and pure cerium oxide (CeO_2) powder (99.9 pct purity, average size 7 μm). Powder mixtures of Al-5 mol pct CeO_2 were ball milled for 1 hour in a water-cooled attritor at 150 rpm, in order to disperse the oxide particles uniformly. The weight ratio of the ball to the powder was 15:1. The ball-milled powders were cold compacted to a billet of $12 \times 12 \times 88$ mm^3 in a steel die using a pressure of 400 MPa. Before FSP, the green compact was sintered in argon for 1 hour at temperatures ranging from 813 to 883 K.

Based upon a preliminary study of this material, a tool rotating speed of 500 rpm in FSP was found to give defect-free specimens consistently. Lower tool rotating speeds often produced specimens with insufficient bonding, while higher tool rotating speeds sometimes caused excessive melting in the specimen. In the present work, the tool rotating speed was set at 500 rpm and the rotating tool was moved along the long axis of the billet with the traversing speed varying from 30 to 120 mm/min. For multiple FSP, the pin tool was moved along the same line and the FSP pass was applied after the workpiece had been cooled from the previous FSP pass. The tool pin used in FSP was a standard M6, and the tool spindle angle (the angle between the spindle and the workpiece normal) was 3 deg. Four FSP passes were applied not only to remove the porosity in the sintered billet but also to enhance the reaction in the specimen.

The X-ray diffraction (XRD) method (Cu K_α, 40 kV, 30 mA) was used to identify the phases present in the specimens. Scanning electron microscopy (SEM) (JSM-6330) was used to study the distribution of second-phase particles. Thin foils for transmission electron microscopy (TEM) were prepared by ion milling. Thin foils were examined using an analytical electron microscope (JEOL* 3010) operated at 200 kV.

*JEOL is a trademark of Japan Electron Optics Ltd., Tokyo.

The mechanical properties of specimens machined from the SZ were evaluated on an Instron 5582 (Instron Corporation, Norwood, MA) universal testing machine with an initial strain rate of 1×10^{-3} s^{-1}. The stress direction was aligned along the traverse direction of the FSP. Cylindrical specimens 4 mm in diameter and 6 mm in length were used for compression tests. The gage sections of the tensile specimens were 3 mm in diameter and 14 mm in gage length. The Young's modulus was calculated by determining the slope of the straight-line portion of the tensile stress-strain curve.

III. RESULTS

A. *Microstructure after Sintering*

Sintering was applied to the cold-compacted billet to provide enough strength to prevent cracking in FSP. In addition, a reaction between Al and CeO_2 may occur during sintering if the temperature is high enough to initiate the reaction. The XRD patterns of the as-sintered specimens with various sintering temperatures are shown in Figure 1. There were only Al and CeO_2 in the cold-compacted billet, and the intensity of the CeO_2 peaks in the as-sintered specimen was reduced as compared to the green compact. In addition, $Al_{11}Ce_3$ and δ^*-Al_2O_3 can be identified in the pattern of the as-sintered specimen, indicating that a partial reaction between the Al and CeO_2 had occurred during sintering.

The microstructure of the sintered specimens was revealed by an SEM secondary electron image (SEI), and the typical microstructure is shown in Figure 2. It indicates that partial reaction between Al and CeO_2 had occurred in local areas during the sintering. The

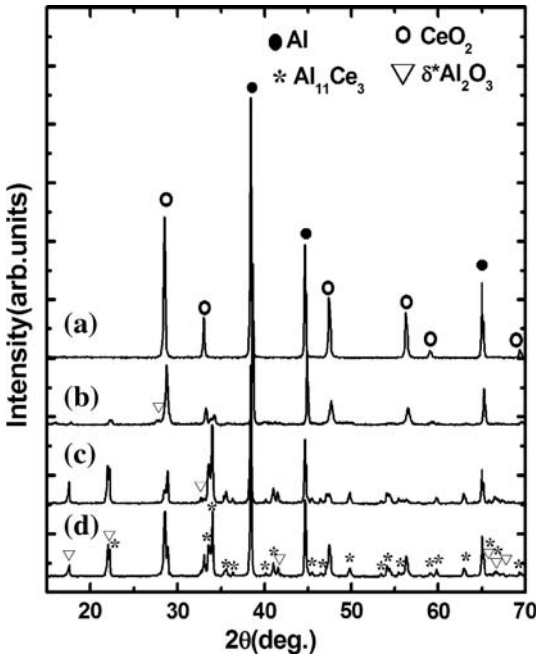

Fig. 1—XRD patterns for green compact and specimens sintered at different temperatures: (*a*) green compact, (*b*) sintered at 813 K, (*c*) sintered at 833 K, and (*d*) sintered at 883 K.

microstructure of the green compact was revealed by SEM SEI, as shown Figure 2(a). The distribution of CeO_2 particles in the green compact is not homogeneous. The bright areas in Figure 2(a) correspond to materials containing a high CeO_2 concentration. The effect of the sintering temperature on the microstructure of the as-sintered specimens is shown in Figures 2(b) through (d). It indicates that a reaction between Al and CeO_2 had occurred in local areas during the sintering. The bulky white phase (marked by C in Figure 2) in the sintered specimens is a Ce-containing compound, mainly $Al_{11}Ce_3$. The aluminum matrix appears in gray, while the black areas are voids due to incomplete sintering. The size of the $Al_{11}Ce_3$ phase increases with increasing sintering temperature. In addition, the gray phase with a rounded appearance (marked by A in Figure 2) enclosed by the white phase ($Al_{11}Ce_3$) was identified as an Al-rich phase, presumably Al-$Al_{11}Ce_3$ eutectic. This morphology suggests that local melting and resolidification had occurred.

The chemical reaction between Al and CeO_2 may consist of the following two parts:

$$2Al + 3/2CeO_2 \rightarrow Al_2O_3 + 3/2Ce + \Delta H_1 \qquad [1]$$

$$11Al + 3Ce \rightarrow Al_{11}Ce_3 + \Delta H_2 \qquad [2]$$

Both reactions are exothermic, *i.e.*, $\Delta H_1 = -44.1$ kJ/mol[28] and $\Delta H_2 = -574$ kJ/mol.[29] There is Al-$Al_{11}Ce_3$ eutectic in the Al-rich side of the Al-Ce binary phase diagram, and the eutectic temperature is 913 K.[29] The heat released from the Al-CeO_2 reaction may cause the eutectic melting of Al and $Al_{11}Ce_3$. However, the melting only occurs locally and resolidification follows because the heat is rapidly lost to the surrounding aluminum matrix. It is suggested that the microstructure consisting of round Al-rich phase (marked by A) enclosed by $Al_{11}Ce_3$ may result from the local melting and resolidification of material with a hypereutectic Al-$Al_{11}Ce_3$ composition.

B. *Microstructure after FSP*

The major processing parameters considered in FSP are the tool rotating speed and the tool traversing speed. Based upon preliminary study, the tool rotating speed of 500 rpm was found to give defect-free specimens consistently. To investigate the effect of the traversing speed of the rotating tool, the specimens were sintered at 883 K and followed by four FSP passes with a tool rotating speed of 500 rpm. The XRD patterns of the FSP specimens produced by different tool traversing speeds are shown in Figure 3, which indicates that CeO_2 peaks have disappeared after four FSP passes for all the conditions studied. For FSP specimens produced with tool traversing speeds of 30 and 85 mm/min, the phases can be identified as Al, $Al_{11}Ce_3$, and δ^*-Al_2O_3. This suggests that CeO_2 had reacted completely with Al after four FSP passes in these processing conditions. The δ^*-Al_2O_3 is one of the transition phases of alumina. It has an orthorhombic structure ($a = 0.7934$ nm, $b = 0.7956$ nm, and $c = 1.1711$ nm),[30] which is close to the tetragonal δ phase.[31] The presence of the δ^*-Al_2O_3 phase is verified by the XRD peaks at $2\theta = 17.6$ and 22.1 deg (Figure 3), because these two peaks could not be attributed to the tetragonal δ phase. However, in the XRD pattern of the FSP specimen produced with a higher tool traversing speed (120 mm/min), there are extra peaks present between $2\theta = 25$ to 32 deg, which can be attributed to the presence of Ce_2O_3, in addition to those corresponding to Al, $Al_{11}Ce_3$, and δ^*-Al_2O_3. Apparently, some of the CeO_2 particles were only partially reduced by Al, which may be attributed to the shorter reaction time and lower reaction temperature associated with the higher tool traversing speed (120 mm/min).

The typical microstructures of specimens after 4 FSP passes are revealed by SEM, as shown in Figure 4. The dispersed particles with a round shape and bright contrast are the Ce-containing compound. According to the results of the XRD analysis, these bright particles are mainly $Al_{11}Ce_3$. In the specimen processed with a tool traversing speed of 120 mm/min, Ce_2O_3 may also present. The Al_2O_3 particles were too small to be observed by SEM. Table I shows that the volume fraction of these Ce-containing particles resulted from each processing condition, which was determined from the SEM image analysis. By assuming Al_2O_3 and $Al_{11}Ce_3$ as the only products of this displacement reaction, the volume fraction of each phase was calculated as a function of the fraction of CeO_2 reacted, as shown in Figure 5. If all the CeO_2 powders added are fully reacted with Al, the volume fraction of Al_2O_3 and $Al_{11}Ce_3$ in the composite will be 0.08 and 0.27, respectively. For specimens sintered at 883 K, the volume fraction of Ce-containing particles produced with a tool traversing speed of 30 or 85 mm/min is close to the value

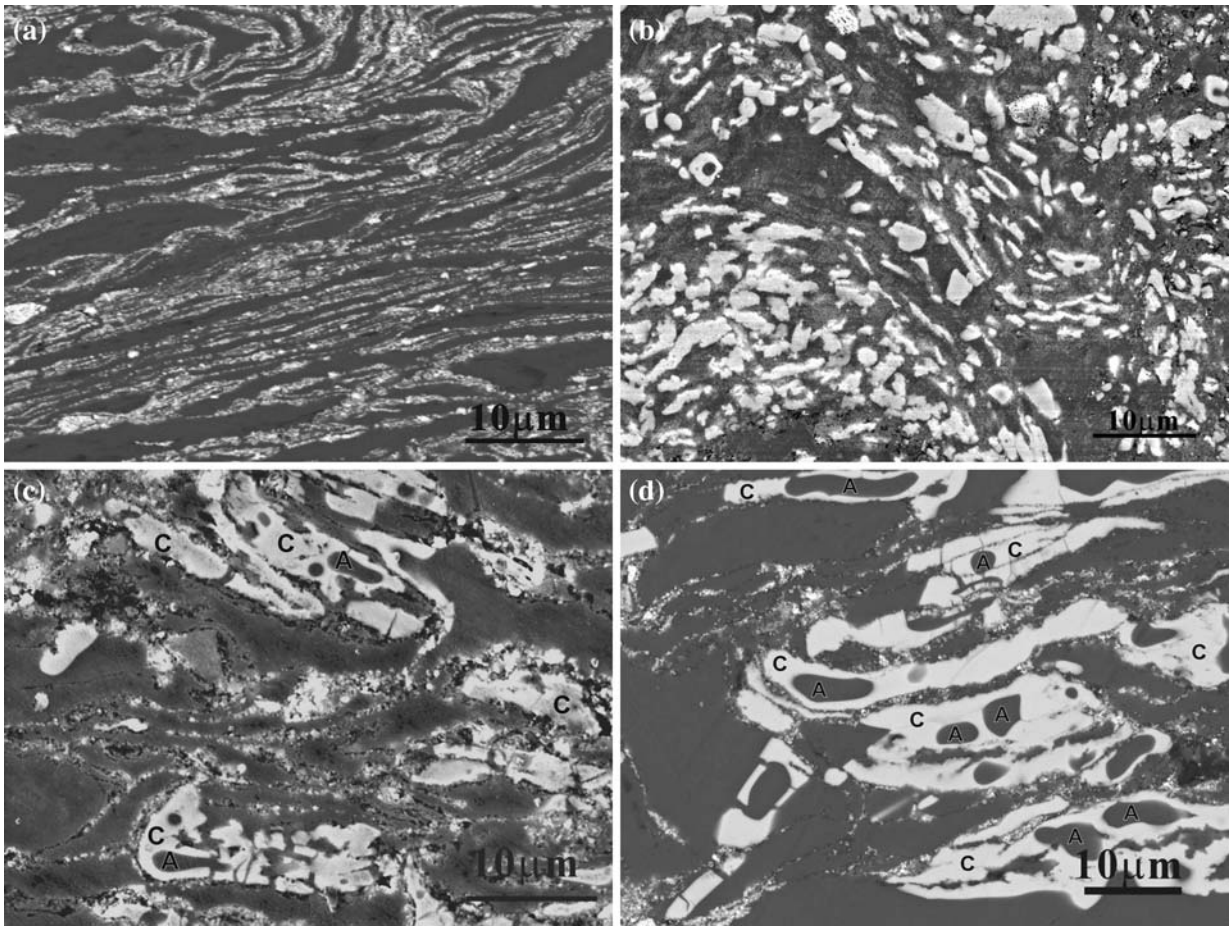

Fig. 2—Effect of sintering temperature on the as-sintered microstructure. The SEM SEIs of (*a*) the green compact specimen, and specimens sintered at (*b*) 813 K, (*c*) 833 K, and (*d*) 883 K. Bulky bright phase (marked by C) in the sintered specimens is a Ce-containing compound, mainly $Al_{11}Ce_3$, and the dark phase with a rounded appearance (marked by A) is an Al-rich phase resulted from eutectic melting and resolidification.

calculated by assuming a complete reaction between Al and CeO_2. However, a tool traversing speed of 120 mm/min could not achieve a complete reaction in four FSP passes for specimens sintered at 883 K. It is also noted from Table I that with a tool traversing speed of 30 mm/min, a complete reaction could be produced by four FSP passes for specimens sintered at temperatures higher than 833 K.

The size distribution of these $Al_{11}Ce_3$ particles resulting from different tool traversing speeds is also shown in Figure 4. It shows that a lower tool traversing speed results in a finer and more uniform particle size. Most of the fine (submicron-sized) particles were believed to be the result of the *in-situ* reaction during FSP, while those particles with a relatively larger size were formed from fragmentation of the bulky $Al_{11}Ce_3$ particles formed during sintering as a result of the severe deformation imposed by FSP. It is suggested that a high traversing speed has less stirring time to refine these particles; therefore, more coarse particles result.

The grain boundaries of the aluminum matrix can be revealed by the use of ion etching, as shown in Figure 6. The average grain size of aluminum matrix in all the specimens is quite similar, approximately 390 to 550 nm, as shown in Table I. In general, the specimen processed by the highest sintering temperature and the lowest tool traversing speed has the largest grain size as compared with specimens prepared by other processing conditions, while the one processed by sintering at 833 K and with a tool traversing speed of 30 mm/min has the smallest grain size.

The microstructure of the FSP specimen was further examined by the use of TEM. The bright-field image in Figure 7(a) shows that nanometer-sized particles are uniformly distributed in the Al matrix. These nanometer-sized particles could be identified as δ^*-Al_2O_3 according to the diffraction rings observed in the corresponding diffraction pattern, as shown in Figure 7(b). Although Al_2O_3 has low mass absorption with respect to electrons, part of the particles still could be observed due to their diffraction contrast. A dark-field image taken from a small portion of the (440) diffraction ring of δ^*-Al_2O_3, as shown in Figure 7(c), can give an example of the distribution of the nanometer-sized particles. The average size of these nanometer-sized particles was determined to be approximately 10 nm, similar to the different processing conditions studied.

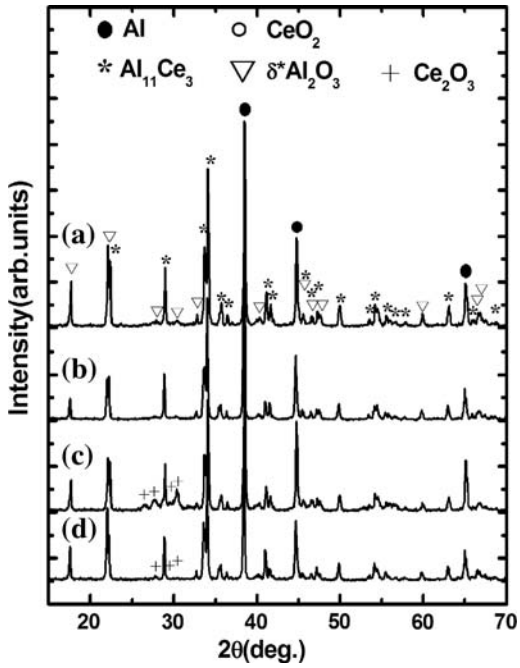

Fig. 3—XRD patterns of FSP specimens processed by different tool traversing speeds. Specimens were sintered at 883 K and followed by four FSP passes. The FSP was performed with a tool rotating at 500 rpm and traversing at (*a*) 30 mm/min, (*b*) 85 mm/min, or (*c*) 120 mm/min. (*d*) Specimen was sintered at 813 K and followed by four FSP passes with tool rotating at 500 rpm and traversing at 30 mm/min.

C. *Mechanical Properties*

The theoretical density for a fully reacted composite was calculated to be 3.19 g/cm^3. The measured density of the composite was 3.26 ± 0.06 g/cm^3. From microscopic observations, the SZ was found to be free of porosity. This evidence indicates that the friction stir processed sample is fully dense. The mechanical properties of the FSP specimen are summarized in Table II. The FSP specimens produced by 30 or 85 mm/min have similar strengths, but those produced by a higher tool traversing speed (120 mm/min) have a lower strength. Increasing the tool traversing speed from 30 to 120 mm/min results in a ~25 pct reduction in the tensile yield stress. The tensile stress-strain curves of FSP specimens produced by different processing conditions are shown in Figure 8. The Young's modulus of the composites is approximately 105 to 109 GPa, which is considerably higher than that of aluminum (70 GPa). This can be attributed to the presence of a large amount of reinforcing particles, $Al_{11}Ce_3$ + Al_2O_3, and to good interfacial bonding for an effective load transfer in the composite. It is also noted that the specimen produced by the high tool traversing speed (120 mm/min) shows a strength lower than those produced by a lower tool traversing speed, and the specimen sintered at low temperature (813 K) also exhibits strength that is relatively lower than those sintered at higher temperatures. These specimens with lower strength may be attributed to the lower amount of reinforcing particles present in them, as shown by the microstructure observations and the results of X-ray analysis. The specimen produced by sintering at 833 K followed by FSP with a tool traversing speed of 30 mm/min possesses the highest strength (ultimate tensile strength (UTS) = 488 MPa), as shown in Table II, because this processing condition results in a complete Al-CeO_2 reaction as well as a microstructure of fine $Al_{11}Ce_3$ particle sizes and Al grain sizes (Table I).

On the other hand, it is noted that the compressive yield strength is higher than the tensile yield strength for each processing condition (Table II). There was no noticeable defect observed in the friction-stir-processed composites. Therefore, the difference between the tensile and the compressive yield strength is unlikely to be attributed to a pre-existing defect. However, the limited tensile ductility may be attributed to the presence of a large amount of reinforcing particles. It is suggested that the difference between the tensile and compressive yield strength may be attributed to the presence of residual stress in the composites.

The microstructure within the gage length of the tensile-tested specimen was further examined by the use of TEM, as shown in Figure 9. From the weak-beam dark-field image, it is seen that dislocations are pinned by fine particles in the aluminum matrix. This clearly demonstrates the operation of the Orowan strengthening mechanism in this composite.

IV. DISCUSSION

A. *In-Situ Reaction in FSP*

In FSP, the time that the material is subjected to the thermomechanical action is very short. The time that the material is affected by the rotating pin in FSP can be considered as the processing time. Based upon the pin diameter and the tool traversing speed, the processing time is estimated to be approximately 3 to 12 seconds for a traversing speed of 120 to 30 mm/min. The rapid *in-situ* reaction may be attributed to the following mechanisms.

(a) A "threshold temperature" is needed to initiate the reaction. The oxide film on Al powders might hinder the reaction. The large plastic strain in FSP[32] can shear the metal powders and break the oxide film surrounding the Al particles, which causes intimate contact between Al and CeO_2. Thus, it is believed that the reaction can be initiated at a lower temperature in FSP than in sintering.
(b) The heat provided by the friction stir of the rotating tool can raise the temperature high enough to initiate the reaction between Al and CeO_2. There is a "synergistic effect" in the reaction, which means that the heat release accompanying the reaction can raise the temperature and promote the reaction.
(c) The Al_2O_3 particles formed at the Al-CeO_2 interface are effectively dispersed in the aluminum matrix by the large plastic strain imposed in FSP. Thus, the reaction at the Al-CeO_2 interface can proceed rapidly. In addition, because the Al_2O_3

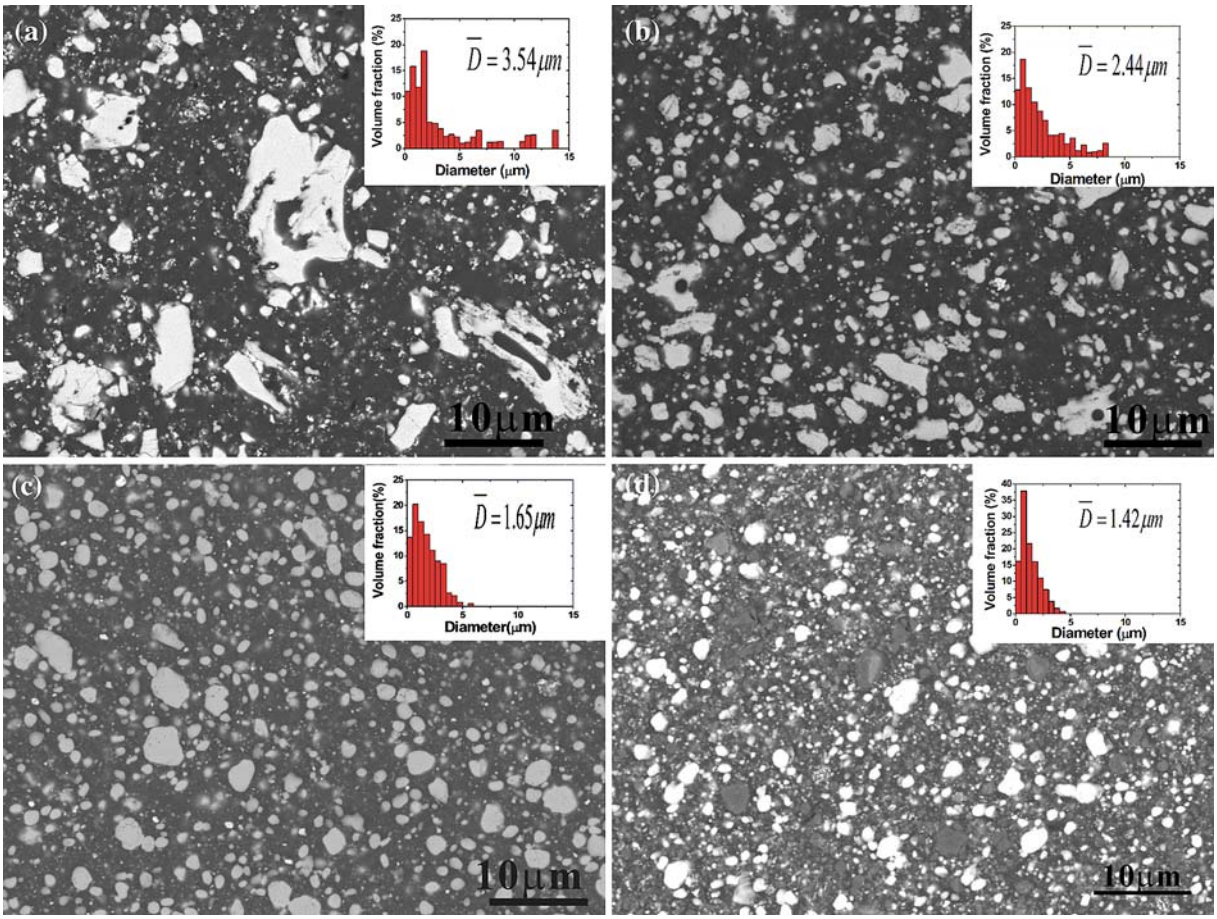

Fig. 4—SEM SEIs showing the microstructure of FSP specimens processed by different tool traversing speeds. Specimens were sintered at 883 K and followed by four FSP passes. The FSP was performed with a tool rotating at 500 rpm and traversing at (*a*) 30 mm/min, (*b*) 85 mm/min, or (*c*) 120 mm/min. (*d*) Specimen was sintered at 833 K and followed by four FSP passes with tool rotating at 500 rpm and traversing at 30 mm/min. Histograms showing the size distribution of $Al_{11}Ce_3$ particles in each specimen are included. The $\overline{D}$ is the average particle size.

Table I. Quantitative Results of Volume Fraction and Average Size of $Al_{11}Ce_3$ Particles and Average Aluminum Grain Size Resulted from Four FSP Passes with a Tool Rotating Speed of 500 rpm and Different Tool Traversing Speeds

Tool Traversing Speed (mm/min)	Volume Fraction of $Al_{11}Ce_3$ Particles	Average Size of $Al_{11}Ce_3$ Particles (μm)	Average Al Grain Size (nm)
30*	0.24	1.42	460
30**	0.27	1.69	390
30†	0.27	1.65	550
85†	0.27	2.44	430
120†	0.22	3.54	480

*Sintered at 813 K.
**Sintered at 833 K.
†Sintered at 883 K.

particles are removed rapidly from the interface, the growth of the particles is limited and nanometer-sized particles result.

Both the FSP parameters and the exothermic reaction will affect the temperature in the sample. Basically, the temperature resulting from the combination of tool rotating and traversing speed must be high enough to initiate the reaction and provide effective consolidation of the sintered billet. It should not be too high, however, because high temperature will promote the exothermic Al-CeO_2 reaction, which may cause excessive melting in the material. The presence of a significant amount of liquid in the material during FSP may result in large cavities in the SZ. Another drawback of a higher FSP temperature is that a coarser microstructure will be produced.

B. *Tensile-Compressive Strength Difference*

The difference between the tensile and compressive yield strength may be attributed to the presence of

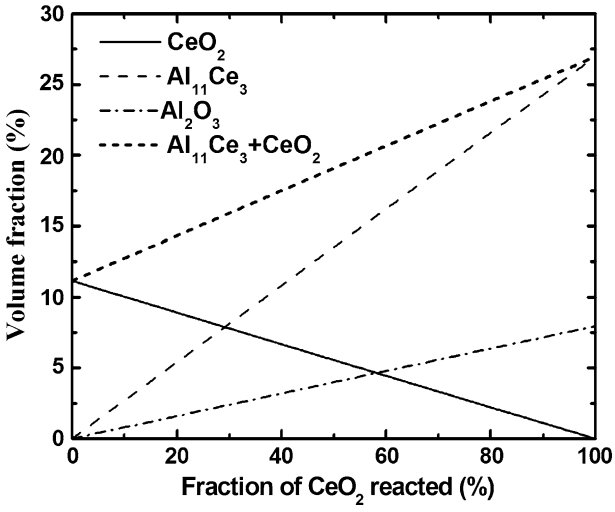

Fig. 5—Calculated volume fraction of each phase as a function of the fraction of CeO_2 reacted.

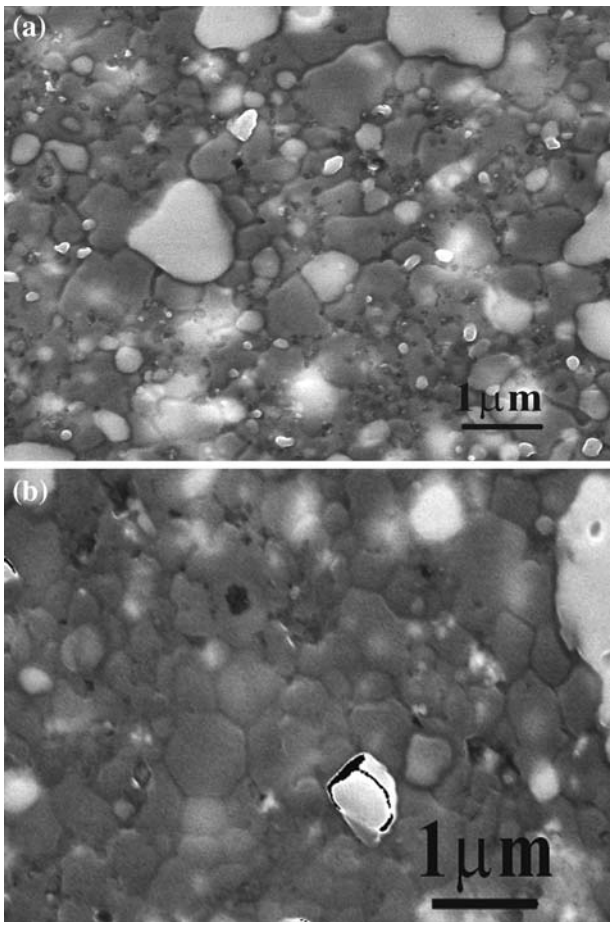

Fig. 6—SEM SEIs of FSP specimens after ion etching to reveal Al grain boundaries. The FSP was performed with tool rotating at 500 rpm and traversing at (*a*) 30 mm/min and (*b*) 120 mm/min.

residual stress in the composites. There are two possible causes for the residual stress in the composites produced by FSP, as follows.

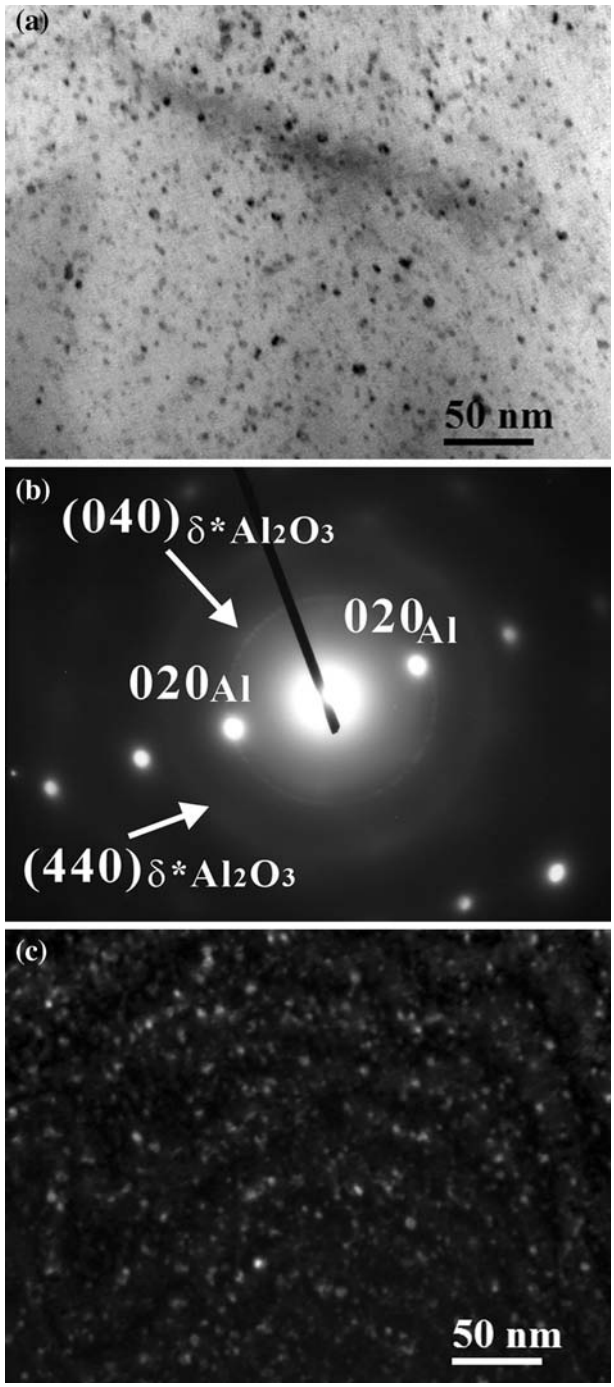

Fig. 7—Microstructure of FSP specimen revealed by TEM. Specimen was sintered at 833 K and followed by four FSP passes with tool traversing at 30 mm/min. (*a*) Bright-field image, (*b*) corresponding electron diffraction pattern, and (c) dark-field image taken from a portion of ∂^*-Al_2O_3 (440) diffraction ring.

(a) The temperature gradient in FSW may result in significant tensile residual stress along the welding direction.[33] This residual stress in the SZ has to be supported by the material surrounding it. Because the testing specimens were machined from the SZ, the residual stress must be relaxed

Table II. Microhardness and Tensile Properties of Specimens Produced by Four FSP Passes with a Tool Rotating Speed of 500 rpm and Different Tool Traversing Speeds

Tool Traversing Speed (mm/min)	Microhardness (Hv)	Young's Modulus (GPa)	Compressive σ_y (MPa)	Tensile E σ_y (MPa)	UTS (MPa)	Tensile Elongation (Pct)
30*	142 ± 3	108 ± 2	373 ± 4	332 ± 5	421 ± 6	4.0 ± 0.9
30**	165 ± 4	109 ± 1	479 ± 12	385 ± 9	488 ± 12	2.8 ± 0.7
30†	141 ± 4	106 ± 2	448 ± 9	379 ± 6	475 ± 4	2.8 ± 0.3
85†	144 ± 5	105 ± 1	431 ± 8	362 ± 3	455 ± 2	3.7 ± 0.7
120†	129 ± 3	106 ± 2	319 ± 1	287 ± 7	398 ± 10	4.4 ± 0.9

*Sintered at 813 K.
**Sintered at 833 K.
†Sintered at 883 K.

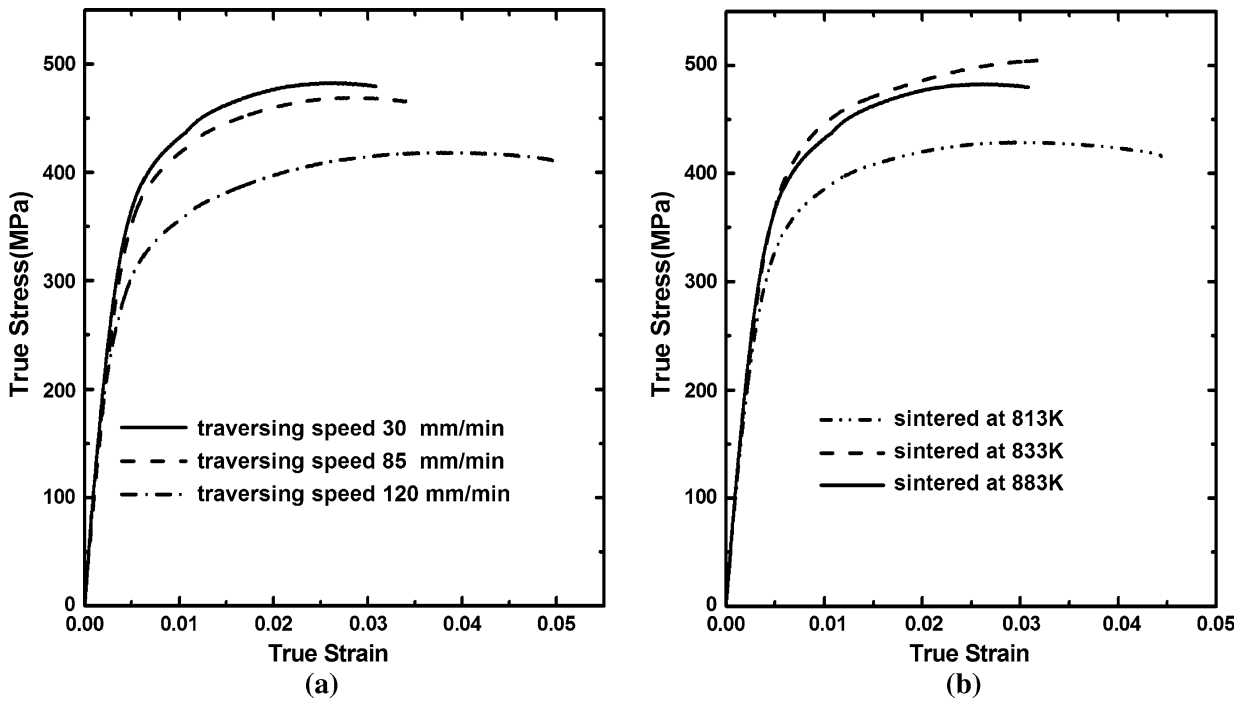

Fig. 8—(*a*) Tensile stress-strain curves for FSP specimens processed by different tool traversing speeds. Specimens were sintered at 883 K and followed by four FSP passes. (*b*) Tensile stress-strain curves for FSP specimens processed by different sintering temperatures. The FSP was performed with tool rotating at 500 rpm and traversing at 30 mm/min, for four FSP passes.

considerably. Therefore, this could not be the major cause for the tension-compression strength difference.

(b) The residual stress may result from the difference in the coefficient of thermal expansion (CTE) between the aluminum matrix and the reinforcing particles ($Al_{11}Ce_3$ and δ^*-Al_2O_3 particles). The CTE of these reinforcing phases is believed to be lower than that of aluminum. When the composite is cooled down from the processing temperature, tensile residual stresses are expected in the aluminum matrix. This means that when the composite is loaded, plastic flow occurs earlier in tension than in compression. Thus, it is believed that the strength difference between compressive and tensile loading can be attributed to the residual stress resulting from the differential contraction between the Al and the reinforcing particles during the cooldown in FSP.

C. *Strengthening Mechanisms*

The high strength of the composite can be attributed to the fine grain size of aluminum matrix as well as the presence of a large amount of fine reinforcing particles. The contribution of the fine grain size to the yield strength can be estimated by the Hall–Petch equation $\Delta\sigma_{gs} = k/\sqrt{d}$, where d is the grain size and $k = 74$ MPa $\mu m^{1/2}$ for pure Al.[34] The average Al grain size of the FSP specimen produced by various processing conditions is in the range of 390 to 550 nm, and therefore $\Delta\sigma_{gs}$ can be calculated as 100 to 118 MPa.

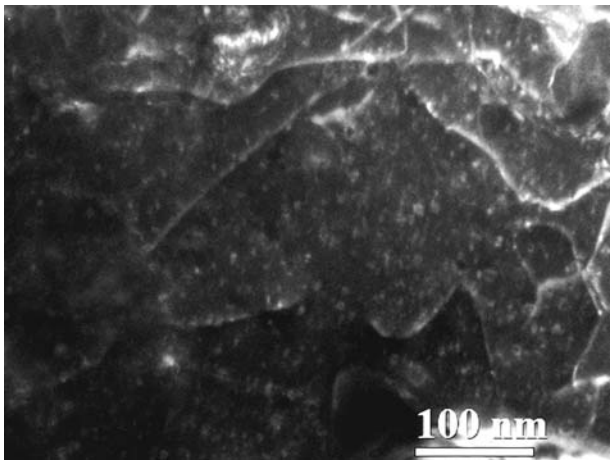

Fig. 9—TEM dark-field image taken from gage length of a tensile-tested specimen, showing that dislocations are pinned by fine particles in the aluminum matrix.

The majority of $Al_{11}Ce_3$ particles have sizes in the same order as aluminum grains. Therefore, they are not supposed to interact directly with intragranular dislocations and cannot contribute to the strength *via* the Orowan bowing mechanism. These particles may contribute to the strength by load sharing. The nanometer-sized particles distributed inside aluminum grains are mainly δ^*-Al_2O_3 particles. The volume fraction V of the Al_2O_3 particles was calculated to be 0.08, and the interparticle spacing λ can then be calculated from the relationship:[35]

$$\lambda = \left[1.25\left(\sqrt{\frac{\pi}{V}}\right) - 2\right]\left(\sqrt{\frac{2}{3}}\right)r \qquad [3]$$

where r is the average radius of the particles. The average particle size $2r$ of the Al_2O_3 particles was determined to be ~10 nm for all the specimens observed, which therefore gives $\lambda = 24$ nm. The contribution of the Al_2O_3 particles to the shear strength can be calculated using the modified Orowan equation given by Martin:[35]

$$\tau_{OR} = \frac{0.81Gb}{2\pi(1-\upsilon)^{1/2}\lambda}\ln\left(2\sqrt{2/3}r\Big/r_o\right) \qquad [4]$$

where G (=26.2 GPa) is the matrix shear modulus, **b** (=0.286 nm) is the Burgers vector, υ (=0.345) is the Poisson's ratio, and r_o (= 4**b**) is the dislocation core radius. The contribution of the Orowan strengthening to the tensile strength can be calculated as $\sigma_{OR} = M\tau_{OR}$, where M is the Taylor factor and $M = 3$ for an fcc polycrystal. The σ_{OR} calculated based upon the microstructural parameters is then approximately 292 MPa. Assuming that the contributions of both the Orowan strengthening and the grain size are linearly additive, the yield strength of FSP specimens with CeO_2 fully reacted can be estimated as 392 to 410 MPa, which is comparable to the experimental yield strength shown in Table II. Additional strength may be contributed by the hard $Al_{11}Ce_3$ particles.

V. CONCLUSIONS

In this study, FSP was applied to produce aluminum-based nanocomposites from powder mixtures of Al-5 mol pct CeO_2. The most important results of this study are summarized as follows.

1. The reinforcing phases were identified as $Al_{11}Ce_3$ and δ^*-Al_2O_3. The average size of the $Al_{11}Ce_3$ particles is approximately 1.4 to 3.5 μm, which depends on the processing parameters used. The Al_2O_3 particles with an average size of ~10 nm were found uniformly distributed in the aluminum matrix. The aluminum matrix of the composite has an ultrafine-grained structure with an average size of approximately 390 to 550 nm.
2. The specimen produced by the high tool traversing speed (120 mm/min) shows a lower strength than those produced by lower tool traversing speeds (30 and 85 mm/min), which can be related to the relatively larger size and lower amount of reinforcing particles produced by the higher tool traversing speed. This may be attributed to the shorter reaction time and lower reaction temperature associated with a higher tool traversing speed.
3. After sintering at temperatures higher than 833 K, four FSP passes with a tool traversing speed of 30 mm/min would result in the CeO_2 being reacted completely.
4. The major contributions to the high strength of the composite are the submicrometer grain structure of aluminum matrix and the Orowan strengthening caused by the fine dispersion of nanometer-sized Al_2O_3 particles inside aluminum grains. With the optimal processing condition, the composite produced possesses enhanced modulus (E = 109 GPa) and strength (UTS = 488 MPa) as well as a tensile ductility of ~3 pct.
5. There is a significant difference between the compressive and tensile strength for each processing condition, which may be attributed to the residual stress resulting from the differential contraction between the Al and the reinforcing particles during the cooldown in FSP.

ACKNOWLEDGMENTS

This research was supported by the National Science Council of the Republic of China, Taipei under Grant No. NSC96-2628-E-110-009-MY3.

REFERENCES

1. R.S. Mishra, M.W. Mahoney, S.X. McFadden, N.A. Mara, and A.K. Mukherjee: *Scripta Mater.*, 2000, vol. 42, pp. 163–68.
2. R.S. Mishra and Z.Y. Ma: *Mater. Sci. Eng., R*, 2005, vol. 50, pp. 1–78.
3. Z.Y. Ma: *Metall. Mater. Trans. A*, 2008, vol. 39A, pp. 642–58.
4. P.B. Berbon, W.H. Bingel, R.S. Mishra, C.C. Bampton, and M.W. Mahoney: *Scripta Mater.*, 2001, vol. 44, pp. 61–66.
5. D. Manisha, J.W. Newkirk, and R.S. Mishra: *Scripta Mater.*, 2007, vol. 56, pp. 541–44.

6. Y.J. Kwon, N. Saito, and I. Shigematsu: *J. Mater. Sci. Lett.*, 2002, vol. 21, pp. 1473–76.
7. Y. Wang, X.L. Shi, R.S. Mishra, and T.J. Watson: *Scripta Mater.*, 2007, vol. 56, pp. 971–74.
8. Y.J. Kwon, N. Saito, and I. Shigematsu: *Scripta Mater.*, 2003, vol. 49, pp. 785–89.
9. C.I. Chang, C.J. Lee, and J.C. Huang: *Scripta Mater.*, 2004, vol. 51, pp. 509–14.
10. Z.Y. Ma, R.S. Mishra, and M.W. Mahoney: *Acta Mater.*, 2002, vol. 50, pp. 4419–30.
11. L.B. Johannes, I. Charit, R.S. Mishra, and R. Verma: *Mater. Sci. Eng., A*, 2007, vol. 464, pp. 351–57.
12. Z.Y. Ma, S.R. Sharam, and R.S. Mishra: *Mater. Sci. Eng., A*, 2006, vol. 433, pp. 269–78.
13. Z.Y. Ma, S.R. Sharam, and R.S. Mishra: *Scripta Mater.*, 2006, vol. 54, pp. 1623–26.
14. K. Nakata, Y.G. Kim, H. Fujii, T. Tsumura, and T. Komazaki: *Mater. Sci. Eng., A*, 2006, vol. 437, pp. 274–80.
15. Z.Y. Ma, A.L. Pilchak, M.C. Juhas, and J.C. Williams: *Scripta Mater.*, 2008, vol. 58, pp. 361–66.
16. R.S. Mishra, Z.Y. Ma, and I. Charit: *Mater. Sci. Eng., A*, 2003, vol. 341, pp. 307–10.
17. C.J. Hsu, P.W. Kao, and N.J. Ho: *Scripta Mater.*, 2005, vol. 53, pp. 341–45.
18. C.J. Hsu, C.Y. Chang, P.W. Kao, N.J. Ho, and C.P. Chang: *Acta Mater.*, 2006, vol. 54, pp. 5241–49.
19. I.S. Lee, P.W. Kao, and N.J. Ho: *Intermetallics*, 2008, vol. 16, pp. 1104–08.
20. C.J. Lee, J.C. Huang, and P.J. Hsieh: *Scripta Mater.*, 2006, vol. 54, pp. 1415–20.
21. D.J. Lloyd: *Int. Mater. Rev.*, 1994, vol. 39, pp. 1–23.
22. J.W. Martin and R.D. Doherty: *Stability of Microstructures in Metallic Systems*, Cambridge University Press, Cambridge, 1976, pp. 234–26.
23. S.C. Tjong and Z.Y. Ma: *Mater. Sci. Eng., R*, 2000, vol. 29, pp. 49–113.
24. L. Mei, R.D. Halldearn, and P. Xiao: *Scripta Mater.*, 1999, vol. 41, pp. 541–48.
25. P. Yu, C.J. Deng, N.G. Ma, M.Y. Yau, and D.H. Ng: *Acta Mater.*, 2003, vol. 51, pp. 3445–54.
26. Z.J. Huang, B.Y. Hua, and J.S. Zhang: *Mater. Sci. Eng.*, 2003, vol. A351, pp. 15–22.
27. S.K. Das and L.A. Davis: *Mater. Sci. Eng.*, 1988, vol. 98, pp. 1–12.
28. W.F. Gale and T.C. Totemeier: *Smithells Metals Reference Book*, 8th ed., Elsevier, Oxford, 2004, pp. 8–24.
29. G. Borzone, G. Cacciamani, and R. Ferro: *Metall. Trans. A*, 1991, vol. 22A, pp. 2119–23.
30. D. Fargeot, D. Mercurio, and A. Dauger: *Mater. Chem. Phys.*, 1990, vol. 24, pp. 299–314.
31. Y.G. Wang, P.M. Bronsveld, and J.M. DeHosson: *J. Am. Ceram. Soc.*, 1998, vol. 81, pp. 1655–60.
32. P. Heurtier, C. Desrayaud, and F. Montheillet: *Mater. Sci. Forum*, 2002, vols. 396–402, pp. 1537–42.
33. M. Peel, A. Steuwer, M. Preuss, and P.J. Withers: *Acta Mater.*, 2003, vol. 51, pp. 4791–4801.
34. C.Y. Yu, P.W. Kao, and C.P. Chang: *Acta Mater.*, 2005, vol. 53, pp. 4019–28.
35. J.W. Martin: *Micromechanisms in Particle Hardened Alloys*, Cambridge University Press, Cambridge, 1980, pp. 60–64.